PHYSICAL REVIEW B **109**, L081404 (2024)

Letter

Tunable unconventional integer quantum Hall effect in two-dimensional Dirac-Weyl systems

Y. J. Jin,[1,2] Y. Xu,[2,3] X. L. Xiao,[4] Z. J. Chen,[5] and H. Xu[2,6,*]

[1] *Guangdong Basic Research Center of Excellence for Structure and Fundamental Interactions of Matter, Guangdong Provincial Key Laboratory of Quantum Engineering and Quantum Materials, School of Physics, South China Normal University, Guangzhou 510006, China*

[2] *Department of Physics & Institute for Quantum Science and Engineering, Southern University of Science and Technology, Shenzhen 518055, People's Republic of China*

[3] *Institute of Micro/Nano Materials and Devices, Ningbo University of Technology, Ningbo 315016, Zhejiang, People's Republic of China*

[4] *Department of Physics, Chongqing University, Chongqing 400044, People's Republic of China*

[5] *Songshan Lake Materials Laboratory, Dongguan 523808, People's Republic of China*

[6] *Quantum Science Center of Guangdong-Hong Kong-Macao Greater Bay Area (Guangdong), Shenzhen 518045, People's Republic of China*

(Received 8 April 2023; revised 29 January 2024; accepted 2 February 2024; published 22 February 2024)

Two-dimensional (2D) Dirac semimetals possess intriguing properties due to their low-energy excitations behaving like Dirac fermions. A hallmark of these materials is the unconventional integer quantum Hall effect (IQHE), originating from the quantized Berry phase of Dirac fermions. Herein, using symmetry analysis, tight-binding models, and numerical calculations, we reveal 2D Dirac-Weyl fermions in inversion symmetry breaking systems that exhibit tunable unconventional IQHE. These unique 2D fermions are characterized by a pair of helical edge states related by time-reversal symmetry $\mathcal{T}$, which connect the projections of a Dirac point and two separate Weyl nodes, indicating that the Dirac and Weyl points are interconnected as a whole. We show that these 2D Dirac-Weyl fermions exhibit a tunable unconventional IQHE, featuring a Hall plateau sequence shifted by three units of $\frac{2e^2}{h}$. The distance between adjacent quantized Hall plateaus can be adjusted by strain, which is a unique feature that distinguishes from what is observed in graphene. Through first-principles calculations, we identify an ideal candidate material for hosting 2D Dirac-Weyl fermions, offering a promising avenue for experimental verification. Our findings open up a door to exploring unconventional IQHE in condensed-matter systems beyond graphene.

DOI: 10.1103/PhysRevB.109.L081404

Introduction. In recent decades, two-dimensional (2D) topological semimetals have gained significant research interest due to distinctive properties stemming from their low-energy excitations. The unique properties of their low-energy excitations make them of fundamental interest and have potential applications in low-dimensional electronics [1–5]. So far, several categories of 2D topological semimetals have been extensively studied, with graphene being a prime example. In the nonrelativistic limit, the low-energy excitations of graphene mimic Dirac fermions with quantized Berry phase, resulting in intriguing properties such as nontrivial edge states, unconventional integer quantum Hall effect (IQHE), Klein paradox, and twisted electronics [6–13], etc.

In the past few years, researchers have extensively explored the properties of Dirac fermions in other 2D systems with non-negligible spin-orbit coupling (SOC). To stabilize the crossing points in the presence of SOC, nonsymmorphic symmetries were introduced [14–22]. As in the three-dimensional (3D) case, robust Weyl (two-fold degenerate) and Dirac (four-fold degenerate) semimetals have been developed. In a 2D SOC Weyl semimetal with broken inversion symmetry ($\mathcal{P}$), there are at least two Weyl nodes related by time-reversal symmetry ($\mathcal{T}$) in the Brillouin Zone (BZ), leading to edge states connecting the projections of two Weyl cones [23,24], as shown in Fig. 1(a). In a 2D Dirac semimetal [14,19,25,26], each Dirac fermion is formed by two Weyl points with opposite Berry phase, resulting in vanishing Berry phase, but two edge states connecting one pair of Dirac fermions [see Fig. 1(b)]. The unconventional IQHE, a hallmark of 2D Dirac fermions, is particularly important for transport phenomena and magnetoelectronic devices [7], where the quantized Berry phase shifts the positions of Hall plateaus compared to those in conventional semiconductor interfaces. In bilayer graphene, the Hall plateaus remain at standard integer positions, but the zero-level plateau is missing [7,9,27–29]. So far, in semiconductor interfaces as well as Dirac and Weyl systems, Hall conductances are quantized to different values, but the distances between adjacent Hall plateaus are typically fixed. It is a challenging and elusive task to manipulate the quantized Hall conductances (filling factors or topological invariants) with different intervals between neighboring quantum plateau steps in condensed matter. Topological states, with their intriguing properties, hold substantial potential for dissipationless electronics and fault-tolerant quantum computing. The ability to easily manipulate topological invariants in realistic materials is crucial for advancing topological switching applications [30,31].

---

[*] xuh@sustech.edu.cn

©2024 American Physical Society

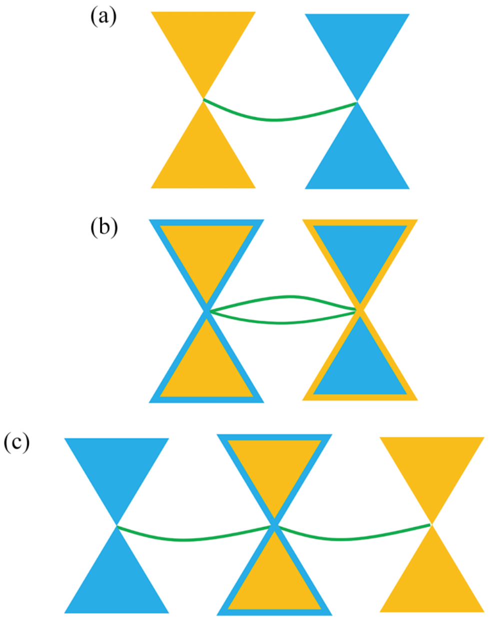

FIG. 1. Various 2D topological semimetals and their edge states. Yellow and light blue colors represent cones with opposite Berry phases. Green lines indicate the corresponding edge states. (a) Dirac points in graphene without SOC or nonsymmorphic symmetry-protected Weyl points with SOC. (b) Dirac points without $\mathcal{P}$ symmetry connected by two edge states. (c) Dirac-Weyl fermions linked by two edge states in a $\mathcal{P}$ symmetry-breaking system.

In this work, we introduce a robust 2D topological state, referred to as the Dirac-Weyl fermion, which serves as a promising platform to realize another type of IQHE and enables manipulation of quantized Hall conductances. Through the analysis of irreducible representations (IRs) in double layer groups, we uncover six layer groups possessing such fermions, as listed in Table I. A notable consequence of our work is that helical edge states connect one Dirac node and two Weyl nodes, resulting in a significant spin Hall conductivity, as depicted in Fig. 1(c). Moreover, our results show that such fermion not only shifts the positions of Hall plateaus by three units of $\frac{2e^2}{h}$ (one unit in graphene) compared to conventional semiconductor interfaces but also offers tunable quantized intervals between adjacent plateaus, signifying the emergence of the tunable unconventional IQHE. Finally, we identify an ideal candidate material for realizing these unique topological fermions, providing a promising platform for investigating unique mesoscopic transport in electronic systems [7] and for the potential application in topological switching transistors [30,31].

TABLE I. Layer groups hosting Dirac-Weyl fermions. The third and fourth columns are the abstract group (AG) and IRs, as indicated in Ref. [33]. The last column shows the symmetry protection of the Dirac-Weyl fermions.

Layer group	Point group	AG	IRs	Symmetry
$P2_12_12$ (21)	D_2	G_{16}^8	R_9R_9	$\{\widetilde{C}_{2x}, \widetilde{C}_{2y}\}=0; T$
$Pba2(25)$	C_{2v}			$\{\widetilde{M}_x, \widetilde{M}_y\}=0; T$
$P42_12$ (54)	D_4	G_{32}^{11}	R_6R_7	$\{\widetilde{C}_{2x}, \widetilde{C}_{2y}\}=0; T$
$P4bm$ (56)	C_{4v}			$\{\widetilde{M}_x, \widetilde{M}_y\}=0; T$
$P\bar{4}2_1m$ (58)	D_{2d}			$\{\widetilde{C}_{2x}, \widetilde{C}_{2y}\}=0; T$
$P\bar{4}b2$ (60)	D_{2d}			$\{\widetilde{M}_x, \widetilde{M}_y\}=0; T$

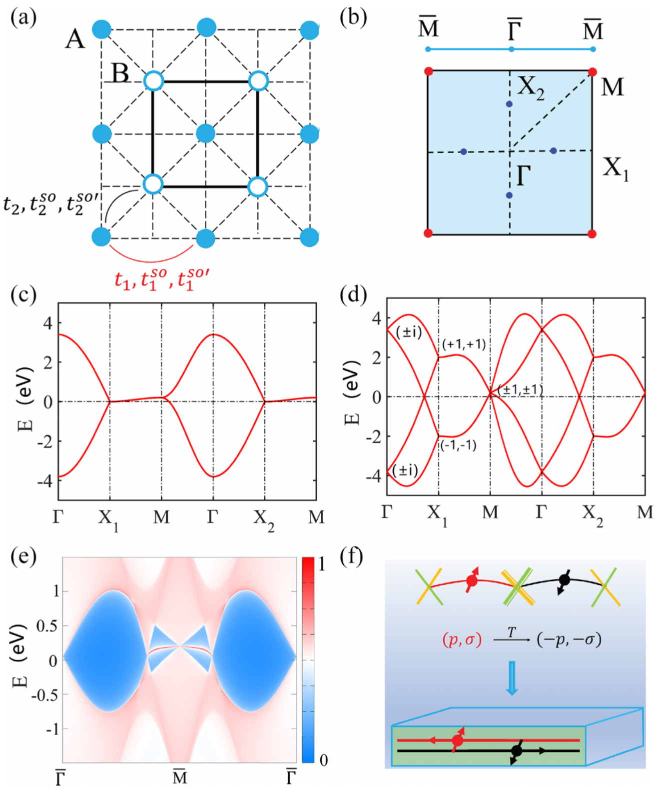

FIG. 2. (a) A 2D square lattice with A (light blue solid circle) and B (light blue hollow circle) sites located at the center and corner of the cell, respectively. The black square represents the unit cell, while the black and red curves illustrate the hopping parameters t_i, t_i^{so}, $t_i^{so'}$ ($i = 1, 2$). (b) The corresponding 2D BZ and its projection onto the (100) edge. The large red dot represents the Dirac point and the small blue dots represent the Weyl points in the BZ. (c) The band structure without SOC along high-symmetry lines. (d) The band structure with SOC along high-symmetry lines, with high-symmetry points labeled by the eigenvalues of $\widetilde{\mathcal{M}}_y$. (e) Edge states computed from a semi-infinite ribbon along the x axis. (f) The schematic diagram of helical edge states in the upper panel and the spin texture related by $\mathcal{T}$ symmetry. The lower panel displays two channels corresponding to two helical edge states with opposite spins propagating in opposite directions. The p and σ denote momentum and spin, respectively.

Tight-binding models and symmetry arguments. Here, we focus on a specific layer group in the main context, while other layer groups are presented in the Supplemental Materials (SM) [32]. First, we construct a four-band tight-binding Hamiltonian for a square lattice with layer group $P4bm$ (No. 56). As shown in Fig. 2(a), the unit cell contains two sites: A (light blue hollow circle) located at the corner and B (light blue solid circle) located at the center. The square 2D BZ, labeled by high-symmetry points and the projected one-dimensional BZ on the (100) edge, are shown in Fig. 2(b). Since the $\mathcal{T}$ symmetry is included, the symmetry group becomes the gray group, which contains one four-fold rotation symmetry C_{4z}^+, two vertical-glide mirror planes,

$\widetilde{\mathcal{M}}_x = \{\mathcal{M}_x|\tau\}$ and $\widetilde{\mathcal{M}}_y = \{\mathcal{M}_y|\tau\}$, as well as $\mathcal{T}$ symmetry, and its combination with all the spatial symmetry elements. Here $\mathcal{M}_x$ and $\mathcal{M}_y$ are mirror reflections perpendicular to the x and y axes, respectively, and $\tau = (\frac{1}{2}, \frac{1}{2}, 0)$ is a half translation of the lattice along the diagonal direction. Both $\widetilde{\mathcal{M}}_x$ and $\widetilde{\mathcal{M}}_y$ interchange the positions of sites A and B. We assume that each lattice site contains an s-like orbital with two spin states. The basis are represented by $|A, \uparrow\rangle$, $|A, \downarrow\rangle$, $|B, \uparrow\rangle$, and $|B, \downarrow\rangle$, and the symmetry generators are consequently represented as

$$\mathcal{C}_{4z}^{+} = \frac{\sqrt{2}}{2}(\sigma_0 - i\sigma_z), \quad \widetilde{\mathcal{M}}_x = -i\tau_x\sigma_x, \quad \mathcal{T} = -i\sigma_y\mathcal{K}, \tag{1}$$

where τ_i and σ_i $(i = x, y, z)$ are Pauli matrices describing the lattice and spin degrees of freedom, respectively, and $\mathcal{K}$ is the complex conjugate operator. The derived tight-binding model is given by

$$\begin{aligned} H =\, & t_1(\cos k_x + \cos k_y) + 2t_2 \cos\frac{k_x}{2}\cos\frac{k_y}{2}\tau_x \\ & + t_1^{so}(\sin k_x\sigma_y - \sin k_y\sigma_x) + t_1^{so'}\tau_z(\sin k_x\sigma_x + \sin k_y\sigma_y) \\ & + 2t_2^{so}\tau_x\left(\sin\frac{k_x}{2}\cos\frac{k_y}{2}\sigma_y - \cos\frac{k_x}{2}\sin\frac{k_y}{2}\sigma_x\right) \\ & + 2t_2^{so'}\cos\frac{k_x}{2}\cos\frac{k_y}{2}\tau_y\sigma_z, \end{aligned} \tag{2}$$

where t_i $(i = 1, 2)$ are hopping parameters, t_i^{so} and $t_i^{so'}$ $(i = 1, 2)$ are SOC terms, and their corresponding bonds are shown in Fig. 2(a). A set of suitable values is chosen as $t_1 = -0.1$, $t_2 = -1.8$, $t_1^{so} = -0.1$, $t_1^{so'} = -1.3$, $t_2^{so'} = -1$, $t_2^{so'} = -0.05$, which can perfectly describe the properties of Dirac-Weyl fermions, including their band structure, edge states, and Landau levels. If the Hamiltonian described in Eq. (2) does not contain SOC, the energy bands form two nodal lines that are two-fold degenerate (four-fold degenerate if spin is considered), as depicted in Fig. 2(c). These nodal lines result from the antiunitary operators $\widetilde{\mathcal{M}}_x\mathcal{T}$ and $\widetilde{\mathcal{M}}_y\mathcal{T}$ at the boundary of the BZ. Here, we focus on the SOC effect, and the corresponding band structure is shown in Fig. 2(d). The nodal lines split into one four-fold Dirac point located at the corners of the BZ and two pairs of two-fold Weyl points along the Γ-X$_1$ and Γ-X$_2$ paths, resulting in a 2D Dirac-Weyl fermion. The Dirac point is denoted by a large red dot, and the Weyl points are indicated by small black dots in Fig. 2(b). Our symmetry analysis reveals that 2D Dirac-Weyl fermions are only determined by the four time-reversal invariant momentum (TRIM) points, namely Γ, X$_1$, X$_2$, and M. At these TRIM points, the selected operators are $\widetilde{\mathcal{M}}_x$, $\widetilde{\mathcal{M}}_y$, and $\mathcal{T}$, but they respect different commutation relations at each TRIM point.

Firstly, we choose the eigenvalues of $\widetilde{\mathcal{M}}_y$ to label the different states at the TRIM points, as shown in Fig. 2(d). At the M point, the three relations $\{\widetilde{\mathcal{M}}_x, \widetilde{\mathcal{M}}_y\}$=0, $\mathcal{T}^2 = -1$, and $(\mathcal{T}\widetilde{\mathcal{M}}_{\mathbf{x}})^2 = -1$ ensure the presence of a four-fold Dirac node. Additional details are available in the SM [32]. In particular, the anticommutation relation between $\widetilde{\mathcal{M}}_x$ and $\widetilde{\mathcal{M}}_y$ leads to two-fold degeneracies, and the two states are always accompanied by their Kramers partners owing to $\mathcal{T}^2 = -1$ and $(\mathcal{T}\widetilde{\mathcal{M}}_{\mathbf{x}})^2 = -1$, ensuring the four-fold Dirac point, as seen in the band structure close to M in Fig. 2(d). When moving to the X$_1$ point, the operators remain unchanged, but the commutation relation between $\widetilde{\mathcal{M}}_x$ and $\widetilde{\mathcal{M}}_y$ changes to $[\widetilde{\mathcal{M}}_x, \widetilde{\mathcal{M}}_y]$=0, resulting in doubly degenerate states at X$_1$. At Γ, $\{\widetilde{\mathcal{M}}_x, \widetilde{\mathcal{M}}_y\}$=0 is maintained, but the product of $\mathcal{T}\widetilde{\mathcal{M}}_{\mathbf{x}}$ becomes $(\mathcal{T}\widetilde{\mathcal{M}}_{\mathbf{x}})^2 = 1$. Thus, only two-fold degeneracies exist at Γ. Between Γ and X$_1$ points, the eigenvalues $\pm i$ evolve into ±1 at X$_1$ because of the half-lattice translation of $\widetilde{\mathcal{M}}_y$, causing band switching and the formation of Weyl points between Γ and X$_1$. To verify the presence of the Dirac point, we construct an effective model at the M point, which is considered as the direct sum of two Weyl equations with opposite chirality (see details in the SM [32]). Our symmetry arguments show that the Dirac-Weyl fermions as a whole are only determined by the symmetry-operator relations at the four TRIM points. This provides a powerful recipe to find Dirac-Weyl fermions in other layer groups. The layer groups that possess 2D Dirac-Weyl fermions are summarized in Table I. We provide a general symmetry analysis and the Hamiltonians for these layer groups to generate the Dirac-Weyl fermions in the SM [32].

Next, we examine the properties of 2D Dirac-Weyl fermions. By using the Green's function method on a semi-infinite ribbon model, we show the existence of edge states in Fig. 2(e). There is one pair of helical edge states with opposite spin textures located at opposite momenta, connecting the projections of one Dirac point and two Weyl points (refer to the spin texture of edge states in Fig. S1 in the SM [32]). Related by $\mathcal{T}$ symmetry, the two helical edge states with opposite spin are degenerate and propagate in opposite directions, potentially leading to a robust large spin Hall conductivity. These spin-momentum locked-edge states offer the possibility of utilizing low-dissipation electronic devices, as illustrated in Fig. 2(f).

Laudau levels and tunable unconventional IQHE. To gain a deeper understanding of Dirac-Weyl fermions, we examine their Landau levels and Hall conductance using the Hamiltonian in Eq. (2). We apply a uniform external magnetic field perpendicular to the plane of the 2D square lattice. Further details of the calculations can be found in the SM [32]. The Landau levels near the Dirac(Weyl) nodes can be expressed as $E(n_{D(W)}) = \sqrt{2|n_{D(W)}|}\nu_{D(W)}/l_B$, where $l_B = \sqrt{c/eB}$ is the magnetic length, $\nu_{D(W)}$ is the Fermi velocity, and $n_{D(W)}$ is the Landau level index [6]. The subscripts D and W denote the Dirac and Weyl nodes in our model, respectively. The calculated Landau level of Dirac-Weyl fermions is characterized by a level anomaly at $n_{D(W)} = 0$ due to its linear dispersion, as shown in Figs. 3(a) and 3(c). We calculate the Hall conductance using the Landauer-Buttiker formula for a six-terminal device, which takes an unconventional form, as given in

$$\sigma_{xy}(E_F) = \frac{2e^2}{h}[2n_D(E_F) + 1] + \frac{2e^2}{h}[4n_W(E_F) + 2], \tag{3}$$

where $2e^2/h$ represents the unit of conductance considering the spin degree of freedom. Interestingly, when the Fermi velocities of Dirac and Weyl fermions are equal $(\nu_D = \nu_W)$, the first Hall conductance is shifted by 3 units of $2e^2/h$, and the adjacent Hall plateaus become 6 units of $2e^2/h$. The Hall conductance of Dirac-Weyl fermions possess a reduced

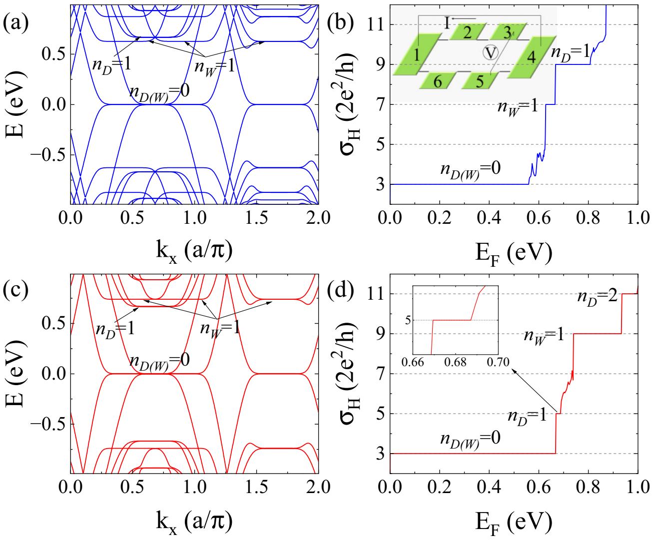

FIG. 3. (a) Landau levels of a ribbon under an external vertical magnetic field and (b) the corresponding Hall conductance of the six-terminal Hall bar with $t_2 = -0.5$. For simplicity, the other parameters used in the calculations are $t_1 = 0$, $t_1^{so} = 0$, $t_1^{so'} = -1.3$, $t_2^{so'} = -1$, $t_2^{so'} = 0$. The inset illustrates the schematic diagram of the six-terminal Hall bar used to determine the Hall conductance numerically. (c) Landau levels of the ribbon under an external vertical magnetic field and (d) the corresponding Hall conductance of the six-terminal Hall bar with $t_2 = -1.8$. The remaining parameters are unchanged from (b). The inset magnifies the region around $n_D = 1$ of the Hall conductance.

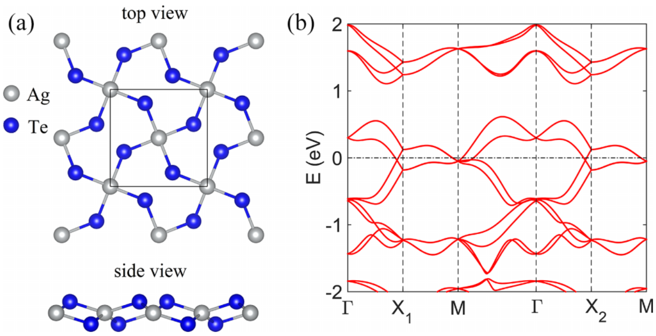

FIG. 4. (a) Monolayer structure of AgTe$_2$. Silver and blue spheres represent Ag and Te atoms, respectively. The unit cell is enclosed in a black square box. (b) Band structure of AgTe$_2$ with SOC obtained by *ab initio* calculations.

form $\sigma_{xy} = 2ne^2/h$ with $n = \pm 3, \pm 9, \pm 15, \ldots$, as shown in Figs. 3(b) and 3(d). These features differ from the unconventional quantization in graphene, where the quantum plateau steps are $n = \pm 1, \pm 3, \pm 5, \ldots$ and in bilayer graphene, where the Hall quantum plateau steps are $n = \pm 2, \pm 4, \pm 6, \ldots$. This is due to the multiple valleys in the model, as seen in the Hall conductance given by Eq. (3). The first term is assigned to the Dirac node with a two-valley degeneracy, and the second term is attributed to the Weyl nodes, taking into account the quadruple valley degeneracy. Therefore, the Hall conductance intervals are featured with 6 units of $2e^2/h$.

As discussed above, the Dirac-Weyl fermions form a coherent system that goes beyond the coupling of two Weyl fermions or a semi-Dirac fermion [9,34]. The Fermi velocities of Dirac and Weyl fermions can be controlled by adjusting the strength of the nearest-neighbor hopping term t_2. When the Fermi velocities of Dirac and Weyl fermions are different, the Landau level intervals are altered, as shown in Figs. 3(a) and 3(c). Consequently, the Hall conductance exhibits additional plateaus with tunable intervals. Specifically, when the Fermi velocity of the Dirac cone is greater than that of the Weyl cones, the Hall conductance of the Dirac-Weyl fermions exhibits quantum plateau steps as $n = \pm 3, \pm \mathbf{5}, \pm 9, \pm \mathbf{11}, \pm 15 \ldots$, as shown in Fig. 3(b). On the other hand, when the Fermi velocity of the Dirac cone is smaller than that of the Weyl cones, the Hall conductance plateau steps becomes $n = \pm 3, \pm \mathbf{7}, \pm 9, \pm \mathbf{13}, \pm 15 \ldots$, as shown in Fig. 3(d). This manipulation can be achieved through experiments that induce strain or deformation. The slight energy separation and quantum interference between the Landau levels of the Dirac and Weyl cones are responsible for the fluctuations in the Hall conductance curve [35]. In contrast, the Hall conductance of graphene depends solely on an external strong magnetic field [7], and does not allow for strain-controlled quantized Hall conductance due to the degeneracy of Dirac cones, which hinders separate velocity adjustments for different cones. Our Dirac-Weyl fermion system introduces an innovative approach for manipulating quantized Hall plateaus (topological invariants) by utilizing external strain instead of a strong magnetic field.

Materials realization. Based on our first-principles calculations, we have identified monolayer square AgTe$_2$ as a promising 2D Dirac-Weyl semimetal candidate. This material belongs to the layer group $P\bar{4}2_1m$ and consists of three atomic layers. The top and bottom layers are composed of Te atoms, while the middle layer contains Ag atoms, as shown in Fig. 4(a). The optimized lattice parameters and Wyckoff positions of Ag and Te atoms can be found in Table I of the SM [32]. To verify the stability of the monolayer AgTe$_2$, we calculate its phonon spectrum and find no imaginary frequencies. Further details on the phonon spectrum analysis can be found in the SM [32].

The electronic band structure of AgTe$_2$ with SOC is shown in Fig. 4(b). There are two pairs of two-fold Weyl points located along the Γ-X$_1$ and Γ-X$_2$ lines with identical energies. Additionally, a single four-fold degenerate Dirac point exists near the M point, forming the Dirac-Weyl fermions in the vicinity of the Fermi level. According to the abstract group [33], the little group at the M point has a four-dimensional (4D) IR formed by two 2D IRs under $\mathcal{T}$ symmetry, thereby ensuring the presence of the four-fold Dirac point. On the high-symmetry lines, the 4D IR splits into two 2D IRs, which is consistent with our symmetry analysis and tight-binding model. Additionally, by applying biaxial strain, we can adjust the Fermi velocities of Dirac and Weyl cones in AgTe$_2$, with summarized results in Table S2 and Fig. S4 in the SM [32]. These findings indicate that biaxial strain can reverse the velocities of Dirac and Weyl nodes, potentially enabling the experimental realization of tunable unconventional IQHE in the realistic material AgTe2.

Conclusions. In summary, using symmetry analysis and numerical calculations, we have provided a recipe for realizing 2D Dirac-Weyl fermions in various layer groups without $\mathcal{P}$ symmetry. Moreover, the 2D Dirac-Weyl fermions serving as a promising platform can realize new types of unconventional IQHE, in which the quantized Hall conductances can be manipulated by strain and deformation. Using first-principles calculations, we identify monolayer $AgTe_2$ as an ideal material for experimental investigations of this phenomenon. Our findings pave the way for further exploration into tunable unconventional IQHE, presenting significant opportunities for advances in magnetoelectronic device technology. Additionally, our results lay the groundwork for the development of topological switching applications, akin to transistor switching, but facilitated through innovative strain engineering.

Acknowledgments. We would like to express our gratitude to Professor J. F. Liu and Professor J. Wang for their valuable discussions and insights. This work was supported by the National Key R&D Program of China (Grant No. 2022YFA1403700), the Shenzhen Science and Technology Program (Grant No. RCYX20200714114523069), the National Natural Science Foundation of China (Grant No. 12374182), Scientific Research Starting Foundation of Ningbo University of Technology (Grant No. 2022KQ51), China Postdoctoral Science Foundation, (Grant No. 2023M743783) and the Center for Computational Science and Engineering at Southern University of Science and Technology.

Y.J.Jin and Y. Xu equally contributed to this work.

---

[1] K. S. Novoselov, A. K. Geim, S. V. Morozov, D. Jiang, Y. Zhang, S. V. Dubonos, I. V. Grigorieva, and A. A. Firsov, Science **306**, 666 (2004).

[2] A. K. Geim, Science **324**, 1530 (2009).

[3] C. L. Kane and E. J. Mele, Phys. Rev. Lett. **95**, 146802 (2005).

[4] A. K. Geim and K. S. Novoselov, Nat. Mater. **6**, 183 (2007).

[5] C. L. Kane and E. J. Mele, Phys. Rev. Lett. **95**, 226801 (2005).

[6] A. H. Castro Neto, F. Guinea, N. M. R. Peres, K. S. Novoselov, and A. K. Geim, Rev. Mod. Phys. **81**, 109 (2009).

[7] Y. Zhang, Y.-W. Tan, H. L. Stormer, and P. Kim, Nature (London) **438**, 201 (2005).

[8] M. I. Katsnelson, K. S. Novoselov, and A. K. Geim, Nat. Phys. **2**, 620 (2006).

[9] K. S. Novoselov, E. McCann, S. Morozov, V. I. Fal'ko, M. Katsnelson, U. Zeitler, D. Jiang, F. Schedin, and A. Geim, Nat. Phys. **2**, 177 (2006).

[10] D. Xiao, M.-C. Chang, and Q. Niu, Rev. Mod. Phys. **82**, 1959 (2010).

[11] N. M. R. Peres, Rev. Mod. Phys. **82**, 2673 (2010).

[12] Y. Cao, V. Fatemi, A. Demir, S. Fang, S. L. Tomarken, J. Y. Luo, J. D. Sanchez-Yamagishi, K. Watanabe, T. Taniguchi, E. Kaxiras *et al.*, Nature (London) **556**, 80 (2018).

[13] Y. Cao, V. Fatemi, S. Fang, K. Watanabe, T. Taniguchi, E. Kaxiras, and P. Jarillo-Herrero, Nature (London) **556**, 43 (2018).

[14] S. M. Young and C. L. Kane, Phys. Rev. Lett. **115**, 126803 (2015).

[15] Z. Wang, A. Alexandradinata, R. J. Cava, and B. A. Bernevig, Nature (London) **532**, 189 (2016).

[16] B. J. Wieder and C. L. Kane, Phys. Rev. B **94**, 155108 (2016).

[17] B. J. Wieder, B. Bradlyn, Z. Wang, J. Cano, Y. Kim, H.-S. D. Kim, A. M. Rappe, C. Kane, and B. A. Bernevig, Science **361**, 246 (2018).

[18] S. A. Parameswaran, A. M. Turner, D. P. Arovas, and A. Vishwanath, Nat. Phys. **9**, 299 (2013).

[19] Y. J. Jin, B. B. Zheng, X. L. Xiao, Z. J. Chen, Y. Xu, and H. Xu, Phys. Rev. Lett. **125**, 116402 (2020).

[20] J. Kruthoff, J. de Boer, J. van Wezel, C. L. Kane, and R.-J. Slager, Phys. Rev. X **7**, 041069 (2017).

[21] W. Wu, Y. Jiao, S. Li, X.-L. Sheng, Z.-M. Yu, and S. A. Yang, Phys. Rev. Mater. **3**, 054203 (2019).

[22] W. Meng, Y. Liu, W.-W. Yu, X. Zhang, and G. Liu, Mater. Today Phys. **27**, 100774 (2022).

[23] P. G. Matveeva, D. N. Aristov, D. Meidan, and D. B. Gutman, Phys. Rev. B **99**, 075409 (2019).

[24] S. Guan, Y. Liu, Z.-M. Yu, S.-S. Wang, Y. Yao, and S. A. Yang, Phys. Rev. Mater. **1**, 054003 (2017).

[25] S. Li, Y. Liu, Z.-M. Yu, Y. Jiao, S. Guan, X.-L. Sheng, Y. Yao, and S. A. Yang, Phys. Rev. B **100**, 205102 (2019).

[26] J. Wang, Phys. Rev. B **95**, 115138 (2017).

[27] K. v. Klitzing, G. Dorda, and M. Pepper, Phys. Rev. Lett. **45**, 494 (1980).

[28] V. P. Gusynin and S. G. Sharapov, Phys. Rev. Lett. **95**, 146801 (2005).

[29] T. Taychatanapat, K. Watanabe, T. Taniguchi, and P. Jarillo-Herrero, Nat. Phys. **7**, 621 (2011).

[30] X. Qian, J. Liu, L. Fu, and J. Li, Science **346**, 1344 (2014).

[31] E. J. Sie, C. M. Nyby, C. Pemmaraju, S. J. Park, X. Shen, J. Yang, M. C. Hoffmann, B. Ofori-Okai, R. Li, A. H. Reid *et al.*, Nature (London) **565**, 61 (2019).

[32] See Supplemental Material at http://link.aps.org/supplemental/10.1103/PhysRevB.109.L081404 for details on the symmetry analysis of the 2D Dirac-Weyl fermions, the lattice models for layer groups $Pba2$, $P4bm$, $P\bar{4}b2$, $P2_12_12$, $P42_12$, and $P\bar{4}2_1m$, the Landauer-Buttiker formula utilized to calculate the conductance, and the computational details for first-principles calculations; see also Refs [36–47] cited therein.

[33] C. Bradley and A. Cracknell, *The Mathematical Theory of Symmetry in Solids* (Clarendon Press, Oxford, 1972).

[34] P. Sinha, S. Murakami, and S. Basu, Phys. Rev. B **102**, 085416 (2020).

[35] J. Wang, H. B. Sun, and D. Y. Xing, Phys. Rev. B **69**, 085304 (2004).

[36] S. Datta, *Electronic Transport in Mesoscopic Systems* (Cambridge University Press, Cambridge, 1997).

[37] P. Hohenberg and W. Kohn, Phys. Rev. **136**, B864 (1964).

[38] W. Kohn and L. J. Sham, Phys. Rev. **140**, A1133 (1965).

[39] G. Kresse and J. Furthmüller, Phys. Rev. B **54**, 11169 (1996).

[40] G. Kresse and J. Furthmüller, Comput. Mater. Sci. **6**, 15 (1996).

[41] P. E. Blöchl, Phys. Rev. B **50**, 17953 (1994).

[42] J. P. Perdew, K. Burke, and M. Ernzerhof, Phys. Rev. Lett. **77**, 3865 (1996).

[43] R. Elmér, M. Berg, L. Carlén, B. Jakobsson, B. Norén, A. Oskarsson, G. Ericsson, J. Julien, T. F. Thorsteinsen, M. Guttormsen, G. Løvhøiden, V. Bellini, E. Grosse, C. Müntz, P. Senger, L. Westerberg, Phys. Rev. Lett. **78**, 1396(E) (1997).

[44] M. L. Sancho, J. L. Sancho, and J. Rubio, J. Phys. F **14**, 1205 (1984).

[45] Q. Wu, S. Zhang, H.-F. Song, M. Troyer, and A. A. Soluyanov, Comput. Phys. Commun. **224**, 405 (2018).

[46] A. Togo, F. Oba, and I. Tanaka, Phys. Rev. B **78**, 134106 (2008).

[47] X. Gonze and C. Lee, Phys. Rev. B **55**, 10355 (1997).